Biomedical Optics EXPRESS

Hemodynamic and morphological vasculature response to a burn monitored using a combined dual-wavelength laser speckle and optical microangiography imaging system

Jia Qin,[1,2] Roberto Reif,[1,2] Zhongwei Zhi,[1] Suzan Dziennis,[1] and Ruikang Wang[1,*]

[1]*Department of Bioengineering, University of Washington, 3720 15th Avenue NE, Seattle, Washington 98195, USA*
[2]*These authors contributed equally to this work*
**wangrk@uw.edu*

Abstract: A multi-functional imaging system capable of determining relative changes in blood flow, hemoglobin concentration, and morphological features of the blood vasculature is demonstrated. The system combines two non-invasive imaging techniques, a dual-wavelength laser speckle contrast imaging (2-LSI) and an optical microangiography (OMAG) system. 2-LSI is used to monitor the changes in the dynamic blood flow and the changes in the concentration of oxygenated (HbO), deoxygenated (Hb) and total hemoglobin (HbT). The OMAG system is used to acquire high resolution images of the functional blood vessel network. The vessel area density (VAD) is used to quantify the blood vessel network morphology, specifically the capillary recruitment. The proposed multi-functional system is employed to assess the blood perfusion status from a mouse pinna before and immediately after a burn injury. To our knowledge, this is the first non-invasive, non-contact and multifunctional imaging modality that can simultaneously measure variations of several blood perfusion parameters.

OCIS codes: (170.6930) Tissue; (040.3060) Infrared; (120.6150) Speckle imaging; (170.4500) Optical coherence tomography; (130.3120) Integrated optics devices.

References and links

1. L. Pascarella, G. W. Schmid Schönbein, and J. J. Bergan, "Microcirculation and venous ulcers: a review," Ann. Vasc. Surg. **19**(6), 921–927 (2005).
2. D. L. Crandall, G. J. Hausman, and J. G. Kral, "A review of the microcirculation of adipose tissue: anatomic, metabolic, and angiogenic perspectives," Microcirculation **4**(2), 211–232 (1997).
3. D. De Backer, J. Creteur, J. C. Preiser, M. J. Dubois, and J. L. Vincent, "Microvascular blood flow is altered in patients with sepsis," Am. J. Respir. Crit. Care Med. **166**(1), 98–104 (2002).
4. S. C. Bondy, R. A. W. Lehman, and J. L. Purdy, "Visual attention affects brain blood flow," Nature **248**(5447), 440–441 (1974).
5. G. Bell and A. M. Harper, "Measurement of regional blood flow through skin from clearance of krypton-85," Nature **202**(4933), 704–705 (1964).
6. D. Attwell, A. M. Buchan, S. Charpak, M. Lauritzen, B. A. Macvicar, and E. A. Newman, "Glial and neuronal control of brain blood flow," Nature **468**(7321), 232–243 (2010).
7. M. Ferrari, T. Binzoni, and V. Quaresima, "Oxidative metabolism in muscle," Philos. Trans. R. Soc. Lond. B Biol. Sci. **352**(1354), 677–683 (1997).
8. V. Provitera, M. Nolano, N. Pappone, E. Lubrano, A. Stancanelli, B. Lanzillo, and L. Santoro, "Axonal degeneration in systemic sclerosis can be reverted by factors improving tissue oxygenation," Rheumatology (Oxford) **46**(11), 1739–1741 (2007).
9. S. R. Nirmala, S. Dandapat, and P. M. Bora, "Wavelet weighted blood vessel distortion measure for retinal images," Biomed. Signal Process. Control **5**(4), 282–291 (2010).
10. G. Ciuffetti, L. Pasqualini, M. Pirro, R. Lombardini, M. De Sio, G. Schillaci, and E. Mannarino, "Blood rheology in men with essential hypertension and capillary rarefaction," J. Hum. Hypertens. **16**(8), 533–537 (2002).
11. P. M. Hutchins, V. L. Roddick, and J. W. Dusseau, "Correlation of blood-pressure and rarefaction of small arterioles in back-crossed spontaneously hypertensive rats," Microvasc. Res. **21**, 246–9999 (1981).

#158016 - $15.00 USD Received 10 Nov 2011; revised 14 Jan 2012; accepted 16 Jan 2012; published 9 Feb 2012

12. J. P. Noon, B. R. Walker, D. J. Webb, A. C. Shore, D. W. Holton, H. V. Edwards, and G. C. M. Watt, "Impaired microvascular dilatation and capillary rarefaction in young adults with a predisposition to high blood pressure," J. Clin. Invest. **99**(8), 1873–1879 (1997).
13. C. M. Wacker, A. W. Hartlep, M. Bock, S. Pfleger, G. Beck, G. van Kaick, L. R. Schad, and W. R. Bauer, "BOLD-MRI of the heart in patients with coronary artery disease: evidence for imaging of capillary recruitment in myocardium supplied by the stenotic artery," Circulation **98**, 371–9999 (1998).
14. F. S. Sutherland, E. Stefansson, D. L. Hatchell, and H. Reiser, "Retinal oxygen consumption in vitro. The effect of diabetes mellitus, oxygen and glucose," Acta Ophthalmol. (Copenh.) **68**(6), 715–720 (1990).
15. W. W. Wagner, Jr., L. P. Latham, and R. L. Capen, "Capillary recruitment during airway hypoxia: role of pulmonary artery pressure," J. Appl. Physiol. **47**(2), 383–387 (1979).
16. P. Horstmann, "The oxygen consumption in diabetes mellitus," Acta Med. Scand. **139**(4), 326–330 (1951).
17. E. Tibiriçá, E. Rodrigues, R. A. Cobas, and M. B. Gomes, "Endothelial function in patients with type 1 diabetes evaluated by skin capillary recruitment," Microvasc. Res. **73**(2), 107–112 (2007).
18. D. Huang, E. A. Swanson, C. P. Lin, J. S. Schuman, W. G. Stinson, W. Chang, M. R. Hee, T. Flotte, K. Gregory, C. A. Puliafito, and J. G. Fujimoto, "Optical coherence tomography," Science **254**(5035), 1178–1181 (1991).
19. S. A. Boppart, B. E. Bouma, C. Pitris, J. F. Southern, M. E. Brezinski, and J. G. Fujimoto, "*In vivo* cellular optical coherence tomography imaging," Nat. Med. **4**(7), 861–865 (1998).
20. L. An and R. K. Wang, "Use of a scanner to modulate spatial interferograms for *in vivo* full-range Fourier-domain optical coherence tomography," Opt. Lett. **32**(23), 3423–3425 (2007).
21. R. K. K. Wang and L. An, "Multifunctional imaging of human retina and choroid with 1050-nm spectral domain optical coherence tomography at 92-kHz line scan rate," J. Biomed. Opt. **16**(5), 050503 (2011).
22. H. F. Zhang, K. Maslov, G. Stoica, and L. V. Wang, "Functional photoacoustic microscopy for high-resolution and noninvasive *in vivo* imaging," Nat. Biotechnol. **24**(7), 848–851 (2006).
23. J. A. Eyre, T. J. H. Essex, P. A. Flecknell, P. H. Bartholomew, and J. I. Sinclair, "A comparison of measurements of cerebral blood flow in the rabbit using laser Doppler spectroscopy and radionuclide labelled microspheres," Clin. Phys. Physiol. Meas. **9**(1), 65–74 (1988).
24. D. A. Boas and A. K. Dunn, "Laser speckle contrast imaging in biomedical optics," J. Biomed. Opt. **15**(1), 011109 (2010).
25. C. Ayata, A. K. Dunn, Y. Gursoy-OZdemir, Z. H. Huang, D. A. Boas, and M. A. Moskowitz, "Laser speckle flowmetry for the study of cerebrovascular physiology in normal and ischemic mouse cortex," J. Cereb. Blood Flow Metab. **24**(7), 744–755 (2004).
26. A. F. Fercher and J. D. Briers, "Flow Visualization by Means of Single-Exposure Speckle Photography," Opt. Commun. **37**(5), 326–330 (1981).
27. J. S. Wyatt, M. Cope, D. T. Delpy, S. Wray, C. Richardson, and E. O. R. Reynolds, "Responses of cerebral vasculature to changes in arterial carbon-dioxide tension measured by near-infrared spectroscopy in newborn-infants," Pediatr. Res. **22**(2), 230–9999 (1987).
28. Z. Luo, Z. Yuan, Y. Pan, and C. Du, "Simultaneous imaging of cortical hemodynamics and blood oxygenation change during cerebral ischemia using dual-wavelength laser speckle contrast imaging," Opt. Lett. **34**(9), 1480–1482 (2009).
29. A. K. Dunn, A. Devor, H. Bolay, M. L. Andermann, M. A. Moskowitz, A. M. Dale, and D. A. Boas, "Simultaneous imaging of total cerebral hemoglobin concentration, oxygenation, and blood flow during functional activation," Opt. Lett. **28**(1), 28–30 (2003).
30. B. J. Vakoc, R. M. Lanning, J. A. Tyrrell, T. P. Padera, L. A. Bartlett, T. Stylianopoulos, L. L. Munn, G. J. Tearney, D. Fukumura, R. K. Jain, and B. E. Bouma, "Three-dimensional microscopy of the tumor microenvironment *in vivo* using optical frequency domain imaging," Nat. Med. **15**(10), 1219–1223 (2009).
31. L. An, J. Qin, and R. K. Wang, "Ultrahigh sensitive optical microangiography for *in vivo* imaging of microcirculations within human skin tissue beds," Opt. Express **18**(8), 8220–8228 (2010).
32. M. Jones, J. Berwick, D. Johnston, and J. Mayhew, "Concurrent optical imaging spectroscopy and laser-Doppler flowmetry: the relationship between blood flow, oxygenation, and volume in rodent barrel cortex," Neuroimage **13**(6), 1002–1015 (2001).
33. R. K. Wang, "Three-dimensional optical micro-angiography maps directional blood perfusion deep within microcirculation tissue beds *in vivo*," Phys. Med. Biol. **52**(23), N531–N537 (2007).
34. R. K. K. Wang and Z. H. Ma, "Real-time flow imaging by removing texture pattern artifacts in spectral-domain optical Doppler tomography," Opt. Lett. **31**(20), 3001–3003 (2006).
35. M. Wojtkowski, V. J. Srinivasan, T. H. Ko, J. G. Fujimoto, A. Kowalczyk, and J. S. Duker, "Ultrahigh-resolution, high-speed, Fourier domain optical coherence tomography and methods for dispersion compensation," Opt. Express **12**(11), 2404–2422 (2004).
36. A. C. Sull, L. N. Vuong, L. L. Price, V. J. Srinivasan, I. Gorczynska, J. G. Fujimoto, J. S. Schuman, and J. S. Duker, "Comparison of spectral/Fourier domain optical coherence tomography instruments for assessment of normal macular thickness," Retina **30**(2), 235–245 (2010).
37. A. F. Fercher, C. K. Hitzenberger, G. Kamp, and S. Y. Elzaiat, "Measurement of Intraocular Distances by Backscattering Spectral Interferometry," Opt. Commun. **117**(1-2), 43–48 (1995).
38. L. An and R. K. Wang, "Full range complex ultrahigh sensitive optical microangiography," Opt. Lett. **36**(6), 831–833 (2011).

#158016 - $15.00 USD Received 10 Nov 2011; revised 14 Jan 2012; accepted 16 Jan 2012; published 9 Feb 2012

39. H. M. Subhash, V. Davila, H. Sun, A. T. Nguyen-Huynh, X. R. Shi, A. L. Nuttall, and R. K. K. Wang, "Volumetric *in vivo* imaging of microvascular perfusion within the intact cochlea in mice using ultra-high sensitive optical microangiography," IEEE Trans. Med. Imaging **30**(2), 224–230 (2011).
40. J. Qin, J. Y. Jiang, L. An, D. Gareau, and R. K. Wang, "*In vivo* volumetric imaging of microcirculation within human skin under psoriatic conditions using optical microangiography," Lasers Surg. Med. **43**(2), 122–129 (2011).
41. L. An and R. K. K. Wang, "*In vivo* volumetric imaging of vascular perfusion within human retina and choroids with optical micro-angiography," Opt. Express **16**(15), 11438–11452 (2008).
42. Y. L. Jia, J. Qin, Z. W. Zhi, and R. K. K. Wang, "Ultrahigh sensitive optical microangiography reveals depth-resolved microcirculation and its longitudinal response to prolonged ischemic event within skeletal muscles in mice," J. Biomed. Opt. **16**(8), 086004 (2011).
43. S. Wray, M. Cope, D. T. Delpy, J. S. Wyatt, and E. O. R. Reynolds, "Characterization of the near infrared absorption spectra of cytochrome aa3 and haemoglobin for the non-invasive monitoring of cerebral oxygenation," Biochim. Biophys. Acta **933**(1), 184–192 (1988).
44. S. J. Kirkpatrick, D. D. Duncan, and E. M. Wells-Gray, "Detrimental effects of speckle-pixel size matching in laser speckle contrast imaging," Opt. Lett. **33**(24), 2886–2888 (2008).
45. A. K. Dunn, H. Bolay, M. A. Moskowitz, and D. A. Boas, "Dynamic imaging of cerebral blood flow using laser speckle," J. Cereb. Blood Flow Metab. **21**(3), 195–201 (2001).
46. C. W. Du, A. P. Koretsky, I. Izrailtyan, and H. Benveniste, "Simultaneous detection of blood volume, oxygenation, and intracellular calcium changes during cerebral ischemia and reperfusion *in vivo* using diffuse reflectance and fluorescence," J. Cereb. Blood Flow Metab. **25**(8), 1078–1092 (2005).
47. T. Kusaka, Y. Hisamatsu, K. Kawada, K. Okubo, H. Okada, M. Namba, T. Imai, K. Isobe, and S. Itoh, "Measurement of cerebral optical pathlength as a function of oxygenation using near-infrared time-resolved spectroscopy in a piglet model of hypoxia," Opt. Rev. **10**(5), 466–469 (2003).
48. M. E. Seaman, S. M. Peirce, and K. Kelly, "Rapid analysis of vessel elements (RAVE): a tool for studying physiologic, pathologic and tumor angiogenesis," PLoS ONE **6**(6), e20807 (2011).
49. H. F. Zhang, K. Maslov, G. Stoica, and L. V. Wang, "Imaging acute thermal burns by photoacoustic microscopy," J. Biomed. Opt. **11**(5), 054033 (2006).
50. H. Schulte, A. Sollevi, and M. Segerdahl, "The distribution of hyperaemia induced by skin burn injury is not correlated with the development of secondary punctate hyperalgesia," J. Pain **5**(4), 212–217 (2004).
51. D. G. Crawford, H. M. Fairchild, and A. C. Guyton, "Oxygen lack as a possible cause of reactive hyperemia," Am. J. Physiol. **197**, 613–616 (1959).
52. J. Schrader, F. J. Haddy, and E. Gerlach, "Release of adenosine, inosine and hypoxanthine from the isolated guinea pig heart during hypoxia, flow-autoregulation and reactive hyperemia," Pflugers Arch. **369**(1), 1–6 (1977).
53. C. Mayeur, S. Campard, C. Richard, and J. L. Teboul, "Comparison of four different vascular occlusion tests for assessing reactive hyperemia using near-infrared spectroscopy," Crit. Care Med. **39**(4), 695–701 (2011).
54. S. Trojan and J. Kapitola, "Reaktivní hyperémie mozku potkana po výskové hypoxii [Reactive hyperemia in the brain of rats after high altitude hypoxia]," Sb. Lek. **92**(4), 97–102 (1990).
55. A. H. Mulder, A. P. J. van Dijk, P. Smits, and C. J. Tack, "Real-time contrast imaging: a new method to monitor capillary recruitment in human forearm skeletal muscle," Microcirculation **15**(3), 203–213 (2008).
56. K. Parthasarathi and H. H. Lipowsky, "Capillary recruitment in response to tissue hypoxia and its dependence on red blood cell deformability," Am. J. Physiol. **277**(6 Pt 2), H2145–H2157 (1999).

1. Introduction

The blood vasculature regulates the blood flow and tissue perfusion, and mediates the delivery of nutrients and oxygen to the living tissue [1]. Blood flow rate, hemoglobin concentration and morphological organization of blood vessels, are important fluid dynamic, biochemical and anatomical parameters that can be quantified [1,2]. Adequate blood flow is a prerequisite for the vasculature to function properly [3–6]. Tissue oxygenation and hemoglobin concentration are sensitive indicators of tissue status [7], e.g., a sudden dip in the tissue oxygenation can be a direct indication of severe conditions such as tissue degeneration [8]. The pathological morphology of the blood vessels, such as blood vessel distortion [9] and rarefaction [10,11] are closely related to a certain abnormal state of living tissue [12]. Therefore, monitoring the changes in the blood flow rate, hemoglobin concentration and tissue morphology, are important for studying vascular physiology [9,12–14].

Usually, the changes of the blood flow, metabolic oxygenation, and vascular morphology occur simultaneously under physiological and pathological conditions. For example, the changes of these parameters occur simultaneously during capillary recruitment [13,15]. Reports have shown that diabetes mellitus patients suffer from absence of capillary reserves, due to the changes in oxygen levels (caused by reduced blood flow) and decreased perfusion [14,16,17]. Taking into consideration that the changes of these parameters are interrelated under specific

#158016 - $15.00 USD Received 10 Nov 2011; revised 14 Jan 2012; accepted 16 Jan 2012; published 9 Feb 2012

physiological and pathological conditions, an overall quantification of their values would enhance our understanding of the hemodynamic and morphological procedures under changes in metabolic demand. For this goal, a multi-functional technique is needed to simultaneously elicit several blood perfusion parameters (changes in blood flow, changes in hemoglobin concentration and changes in vessel morphology).

Optical imaging techniques are sensitive to several optical parameters, such as scattering and absorption, which if combined with the Doppler effect [18–22], allows for the measurement of the changes of blood flow, concentration of hemoglobin, and morphology of blood vessels. Photo-acoustic microscopy (PAM) [22] has the capability for detecting several blood perfusion parameters; however, it requires to be in contact with the sample of interest, which carries risks. Laser Doppler imaging [23] and single wavelength laser speckle contrast imaging (LSCI) [24–26] can measure the relative changes of blood flow, but are not capable of imaging changes in oxygenation and morphology of the microcirculation network with high resolution. Near-infrared spectroscopy (NIRS) can non-invasively measure the changes in hemoglobin oxygenation [27], but is difficult to provide the information about the blood flow and the morphology of the blood vessels.

Dual wavelength laser speckle imaging system (2-LSI) is sensitive to the changes in blood flow and the concentration of hemoglobin [28,29]. Optical microangiography is sensitive to the functional blood vessel micromorphology [30,31]. Therefore, by combining these two techniques into one single system, we would be able to obtain several important physiological parameters that enable the quantification of blood perfusion. The methods for imaging the changes in blood flow, oxyhemoglobin and deoxyhemoglobin concentrations have been reported in [28,29,32]. For example, a laser Doppler flowmetry system has been integrated with near-infrared oxymetry as a dual-wavelength system for simultaneous imaging of blood flow and hemoglobin oxygenation changes induced by cortical transient ischemia in rat brain [28]. However, the 2-LSI is still not sufficient in providing high resolution blood vessel network. Therefore, it would be valuable if the 2-LSI is integrated with a non-contact, non-invasive, high resolution (down to blood-perfused capillaries) optical imaging technique that has an ability to provide more comprehensive information about the vasculature. The optical micro-angiography (OMAG) is such a candidate. OMAG was first proposed in 2007 [33] as a variation of spectral domain optical coherence tomography [34–37], and can provide noninvasive, non-contact, three dimensional and high resolution functional blood flow images of biological tissue based on backscattering properties from moving particles such as red blood cells . The recent development of the OMAG modality was reported in [31,38] to have an ultrahigh system sensitivity to the slow blood flows, down to 4 μm/s, which has been successfully employed to obtain detailed micro-capillary networks of different biological tissues *in vivo*, e.g., retina, skin, brain and cochlea [31,39–42].

In this paper, we propose a newly developed multi-functional imaging system, which can simultaneously extract the information as to the changes in blood flow, concentration of oxy and deoxyhemoglobin and morphological change of the vasculatures. This system integrates a 2-LSI and OMAG into one single imaging system. In the integrated system, the 2-LSI used 780 nm and 825 nm wavelengths to visualize the blood flow rate change, and employed near-infrared oxymetry to extract the concentration changes of hemoglobin [43]. More importantly, the OMAG was used to non-invasively image and determine the morphological change of the blood vessels under specific conditions where metabolic demands change. The performance of the multi-functional imaging system is demonstrated by noninvasively imaging blood vessel networks *in vivo* within mouse pinna before and after a burn injury. The newly developed multi-functional system would be beneficial for studying and diagnosing the microvasculature related diseases.

#158016 - $15.00 USD Received 10 Nov 2011; revised 14 Jan 2012; accepted 16 Jan 2012; published 9 Feb 2012

2. Materials and methods

2.1. Experimental protocol

To demonstrate the imaging capability of the multi-functional imaging system, we performed *in vivo* experiments for visualizing the microcirculatory response in the mouse pinna before and after a burn injury. All experiments were performed on C57BL/6 male mice, approximately two months old. After anesthetizing the animal using 2% isoflurane (0.2L/min O2, 0.8L/min air), the mouse pinna was depilated with a commercial human hair remover lotion (Nair). A thermal burn was created by using a metal bar with a 2.5 mm diameter tip (preheated to 100°C), placed in contact with the depilated skin area for a period of ~1 min. During the burn, the pressure applied to the skin by the metal bar was kept constant. After the burn, the mouse pinna had an intact epidermis and dermis, and tissue carbonization was not visible. Therefore, a partial-thickness burn had been created on the mouse pinna. The mouse pinna was then imaged with both the laser speckle and the optical microangiography system before and immediately after the burn. The animal's body temperature was maintained between 36.6 and 37.2°C, throughout the experiment. The animal was disposed of according to IACUC regulations which was approved by the University of Washington Institutional Animal Care and Use Committee and was in compliance with the guidelines of the National Institutes of Health for care and handling of laboratory animals.

2.2. Dual-wavelength laser speckle imaging (2-LSI) system

The multi-functional imaging system is illustrated in Fig. 1. The 2-LSI system contains two single-mode laser diodes with a wavelength of λ_1 = 780 nm (30 mW) and λ_2 = 825 nm (30 mW). The lasers were modulated with an optical chopper at a frequency of 2 Hz, such that only one laser wavelength was selected at one given time. The two laser beams were aligned via a beam splitter such that they illuminated the same surface area of the sample. The incidence of the laser beam was at a 30° angle from the tissue surface [28] to minimize specular reflection. The diffusely reflected light from the tissue was detected with a CMOS camera (Basler A 504k, 1280 × 1024 pixels) through a zoom lens, which provided an adjustable magnification. The speckle size was set to twice the size of the camera pixels [44], which maximized the contrast of the speckle patterns. This was achieved by setting a magnification of 2.5 and imaging a field of

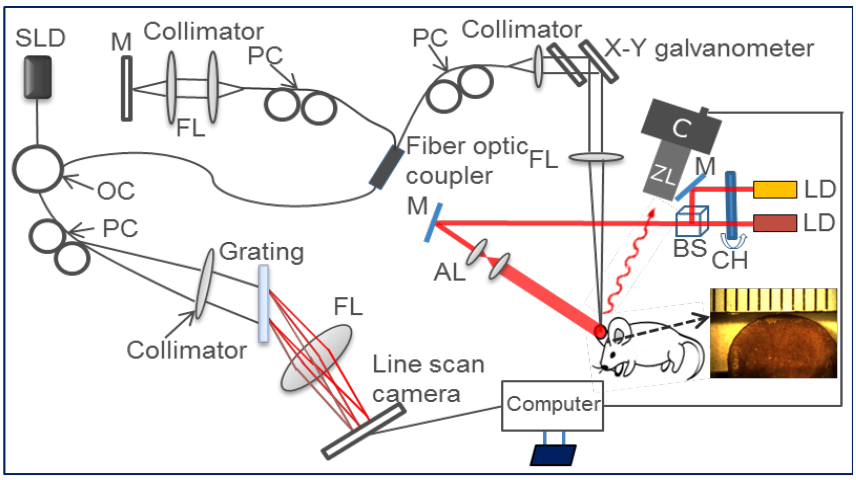

Fig. 1. Schematic diagram of the multi-functional optical imaging system. SLD: superluminescent diode, OC: optical circulator, PC: polarization controller, FL: focusing lens, LD: laser diode, CH: chopper, M: mirror, BS: beam splitter, AL: adjusting lens, C: camera, ZL: zoom lens. The insert is a photo of the mouse pinna. The smallest division on the ruler is 1 mm.

#158016 - $15.00 USD Received 10 Nov 2011; revised 14 Jan 2012; accepted 16 Jan 2012; published 9 Feb 2012

view of ~4 × 4 mm. The camera exposure time was set to 10 ms, to render high contrast images with sufficient dynamic range for speckle flow imaging [28,29].

The 2-LSI system captured 500 frames for each data set. The frame acquisition frequency was set to 2 Hz; therefore, it took ~4 min to capture a data set. After the data was acquired, a five by five pixel binning window was applied on the raw image to reduce noise. The speckle contrast value (K) was calculated as the ratio of standard deviation (σ_s) to the mean intensity of each binning window <I>. The relationship between the speckle contrast and the dynamic features of the speckles is expressed in Eq. (1), where the relative change of blood flow is derived from the model reported in [24,45].

$$K = \frac{\sigma_S}{\langle I \rangle} = \left\{ \frac{\tau_C}{2T} \left[1 - \exp\left(-\frac{2T}{\tau_c} \right) \right] \right\}^{0.5} \quad [1]$$

where T is exposure time of the camera; τ_c is the correlation time, which is assumed to be inversely proportional to a measure of the velocity of the scattering particles.

Changes in the concentration of HbO and Hb can be measured through diffuse reflectance due to the temporal changes of light absorption. Equation (2) is a model based on the Beer-Lambert law [29,46] which extracts the concentration changes of HbO and Hb.

$$\begin{bmatrix} \Delta HbO(t) \\ \Delta Hb(t) \end{bmatrix} = \begin{bmatrix} \varepsilon_{HbO}^{\lambda_1} & \varepsilon_{Hb}^{\lambda_1} \\ \varepsilon_{HbO}^{\lambda_2} & \varepsilon_{Hb}^{\lambda_2} \end{bmatrix}^{-1} \begin{bmatrix} \dfrac{\ln\left(R_{\lambda_1}(0) \big/ R_{\lambda_1}(t) \right)}{L_{\lambda_1}} \\ \dfrac{\ln\left(R_{\lambda_2}(0) \big/ R_{\lambda_2}(t) \right)}{L_{\lambda_2}} \end{bmatrix} \quad [2]$$

where ε is the molar spectral absorbance coefficient of an absorbing chromophore; $R_{\lambda_1}(t)$, $R_{\lambda_2}(t)$ are the measured diffuse reflectance at the two wavelengths after the wound; $R_{\lambda_1}(0)$ and $R_{\lambda_2}(0)$ are the baseline diffuse reflectance values prior to the wound. L_{λ_1} and L_{λ_2} are the path lengths of the light inside the medium and are assumed to be constant, time-invariant and equal to ~1.5 mm [46,47]. The change in the total hemoglobin concentration can be obtained from ΔHbT = ΔHbO + ΔHb and is assumed to be linearly proportional to the local blood volume [29]. To reduce the speckle noise, ten frames were first averaged before the calculation. For the hemoglobin images, no spatial averaging was used.

2.3. Optical Microangiography (OMAG)

A spectral domain optical coherence tomography (SD-OCT) system that implements the OMAG has been developed as previously described. A superluminescent diode with a central wavelength of 1310 nm and a bandwidth of 65 nm was used as an optical coherence tomography (OCT) light source, which yields an axial resolution of ~10 μm in air. The light from the light source was divided into two paths through a 2 × 2 optical coupler, one for the reference arm and the other for the sample arm. In the sample arm, the light was coupled into a custom-designed optical system, containing a collimator, a pair of galvo mirrors, and an objective lens with a 50 mm focal length. This design of the optical system provided a ~20 μm lateral resolution [31]. The light backscattered from the sample and reflected from the reference mirror were recombined using the 2 × 2 optical coupler, and then transmitted to a home-built spectrometer via an optical circulator for the detection of the spectral interference signal. The spectrometer had a spectral resolution of 0.141 nm, providing an imaging depth of 2.22 mm into the sample. A high speed InGaAs line scan camera (SUI, Goodrich Corp) was used in the

#158016 - $15.00 USD Received 10 Nov 2011; revised 14 Jan 2012; accepted 16 Jan 2012; published 9 Feb 2012

spectrometer to capture the interferograms at a recording speed of 92,000 A-lines per second. With this imaging speed, the system sensitivity was determined to be 105 dB at a depth position of 0.5 mm from the zero-delay line. A scanning protocol which yields fast imaging speeds [23] was utilized. Briefly, a saw tooth waveform was used to drive the x-scanner (for fast B scan) and a step function waveform was used to drive the y-scanner (for a 3D scan). Along the x-scanning direction, 256 A-lines were captured with ~8 μm spatial interval between adjacent A-lines to achieve one B-scan cross-sectional image, which covered a range of ~2 mm on the sample. The duty cycle for the rising side of the saw tooth waveform was set at ~80% per cycle, which provided a B-scans frame rate of ~280 frames per second. For the y-scanning direction, the 2 mm scan range was evenly divided into 200 steps with a 10 μm spatial interval between them. In each step, ten frames were captured and processed to extract one B-scan cross-sectional flow image [23]. The system acquired 2000 frames to form each three dimensional data set. The total time for acquiring one 3D data set took ~7 seconds, which is suitable for *in vivo* detection. Thirty five data sets were sequentially acquired in different regions and stitched together to obtain a wide field image that covered an area of ~12 × 8 mm.

The image processing method to obtain images of the microvasculature network probed by OMAG has been reported in [31]. The *en face* projected images were analyzed using a vessel area density (VAD) method, before and after the burn injury [48].

3. Results and discussion

In this section, we first present the dual-wavelength laser speckle imaging results, giving the dynamic information of the changes in blood flow and the changes in the concentrations of Hb, HbO and HbT. Then, the OMAG blood vessel network images are presented, from which the vessel area density is calculated.

3.1. Laser speckle imaging

Figures 2 (A) and (B) present the diffuse reflectance (R(0)) and the speckle contrast image (K) from the control mouse pinna, respectively, and Figs. 2 (C) and (D) present the diffuse reflectance (R(t)) and the speckle contrast image of the mouse pinna after the injury,

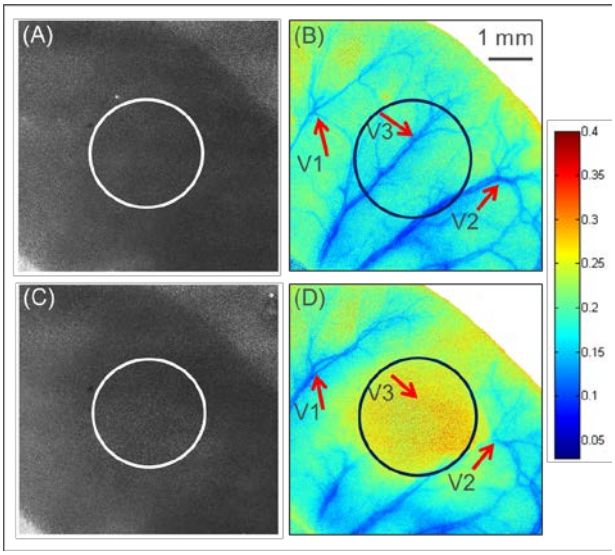

Fig. 2. 2-LSI diffuse reflectance and speckle contrast images of the mouse pinna. (A) Diffuse reflectance, and (B) speckle contrast image of the mouse pinna before the burn. (C) Diffuse reflectance, and (D) speckle contrast image of the mouse pinna after the burn. The circles indicate the burned area. The arrows indicate representative vessels that are affected by the burn injury. Color bar shows the speckle contrast value (K).

#158016 - $15.00 USD Received 10 Nov 2011; revised 14 Jan 2012; accepted 16 Jan 2012; published 9 Feb 2012

respectively. The speckle contrast image was calculated with Eq. (1) using 20 frames. By comparing the diffuse reflectance images (Figs. 2 (A) and (C)), it is not possible to visualize any biological changes caused by the burn injury. However, the speckle contrast images (Figs. 2(B) and (D)) can highlight large blood vessels, and the differences can be observed within the circle region, which represents the injured area. Inside the burn region, the blood flow has decreased after the burn as indicated by an increase in the speckle contrast value. The blood flow changes can be visualized by comparing some representative blood vessels, such as the ones pointed by arrows V1, V2 and V3 in Figs. 2 (B) and (D). Vessels 1 and 2 have an increase and decrease in speckle contrast, respectively, while vessel 3 disappears in Fig. 2 (D).

The speckle contrast images obtained (Figs. 2(B) and 2(D)) were converted to flow images by using Eq. (1) and fitting for τ_c, which is inversely proportional to the velocity of the scattering particles. The subtraction of the flow images (after the injury minus before the injury), normalized by the baseline flow (before the injury), provides the relative change of flow. Figure 3 (A) shows the normalized relative change of blood flow. In general, the flow rate within the injured region decreases, while the flow rate in the surrounding regions increases. For better visualization, we selected three regions of interest (ROI) from the image (marked squares in Fig. 3 (A)). Figure 3 (B) shows the mean and standard deviation of the relative change of blood flow from the three regions. From Fig. 3(B), it can be determined that the blood flow in ROI 2 is reduced, known as haemostasia. The blood flow in the peripheral regions such as ROI 1 has increased, known as hyperaemia. In addition, some regions (e.g., ROI 3) did not present significant blood flow change [49].

To calculate the change in the concentration of HbO and Hb, we employed a model reported in [28] given by Eq. (2), from which HbT was also evaluated. The changes in the concentration of HbO, Hb and HbT are shown in Figs. 3 (C), (E) and (G), respectively. Figures 3 (D), (F) and (H) show the mean and standard deviation of the ROIs 1, 2 and 3. In ROI 1, we can observe that the concentration of HbO decreased, and the concentration of Hb and HbT increased which is consistent with hyperaemia [49,50]. After the increase in blood flow, a brief period of ischemia occurs. Following the ischemia, there is a shortage of oxygen and a buildup of metabolic waste [51–54]. Therefore, it will show that the flow increases and the concentration of oxygenated hemoglobin decreases in the peripheral region of the burn area, such as ROI 1. The thermally coagulated region ROI 2 presented a small decrease in HbO; and a slight increase in Hb and HbT, due to thermal damage of the blood vessels. Although the flow has been reduced, the blood present in ROI2 may have clotted, which would prevent blood from leaving the region and explaining the increase in HbT. ROI 3 had no change in HbO and a small increase in Hb and HbT. We assume that the HbO did not decrease because ROI 3 is still perfused by other main vessels even though V1, V2, and V3 have been affected. We speculate that hypoxia (a condition in which tissues are starved of oxygen) is occurring in these regions, because of the increase of the deoxygenated hemoglobin concentration, and the decrease of the oxygenated hemoglobin concentration.

It is important to mention that the optical properties of the tissue may have been modified due to the injury; therefore, affecting the value of the optical pathlength (Eq. (2). In this study we have assumed this pathlength to be constant; however, this may be a source of error in the results.

3.2. Optical microangiography

Using the OMAG system, we obtained microangiography images of the mouse pinna before and after the burn injury. Figure 4 shows the obtained images after stitching together different regions to produce a ~12 × 8 mm area. It can be observed that the OMAG system has higher resolution compared to the LSI images (Figs. 2(B) and 2(D)), allowing small capillaries to be identified. The three red arrows indicate the vessels (V1, V2 and V3) highlighted in the LSI image (Figs. 2(B) and 2(D)), which can be used as guidelines to compare both the LSI and OMAG images. It is noted that V1, V2 and V3 appear to be vessel pairs (artery and vein) in the

#158016 - $15.00 USD Received 10 Nov 2011; revised 14 Jan 2012; accepted 16 Jan 2012; published 9 Feb 2012

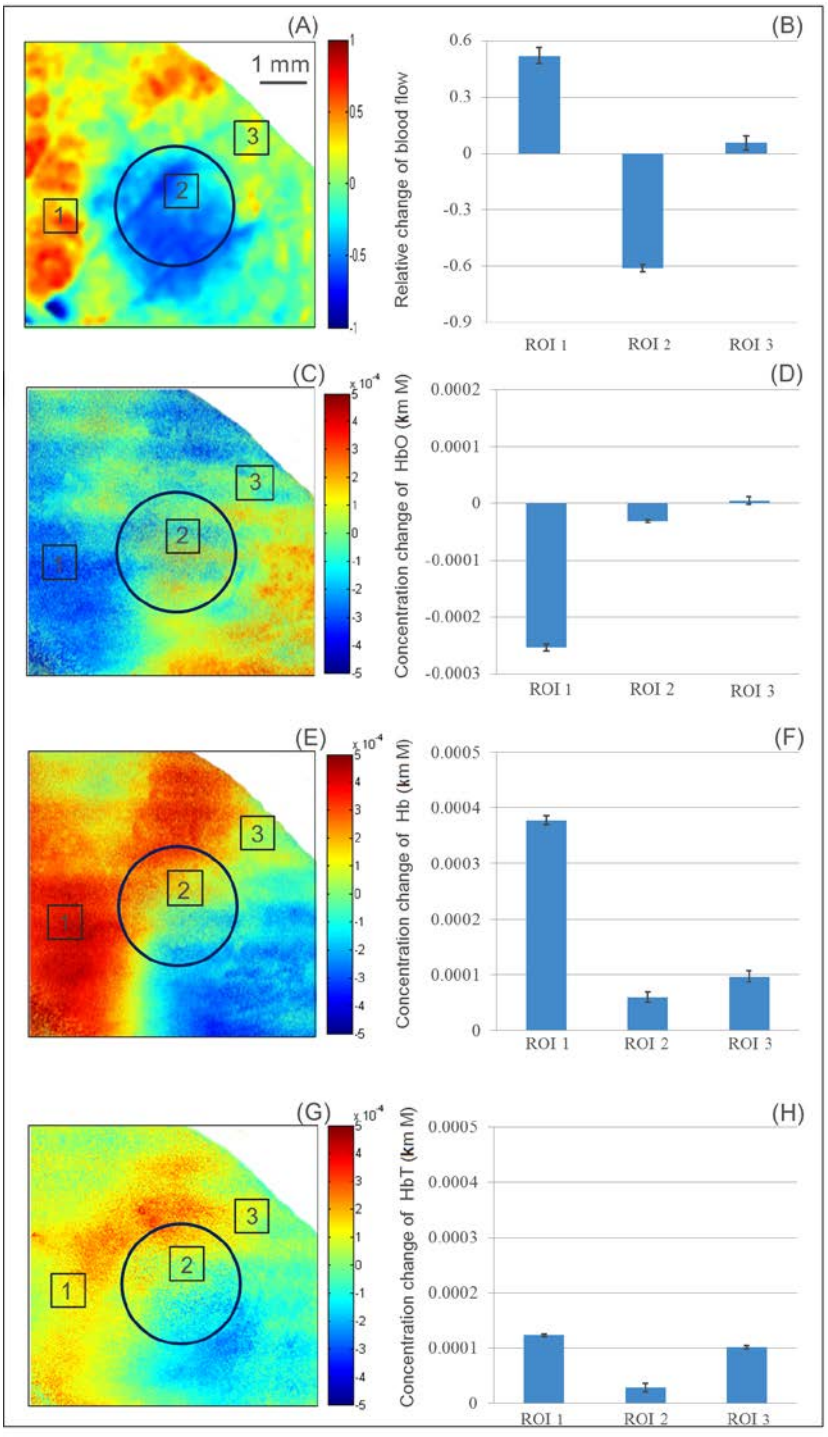

Fig. 3. Color coded map of the relative change of blood flow (A), HbO (C), Hb (E) and HbT (G). Mean and standard deviations of the relative change of blood flow (B), HbO (D), Hb (F) and HbT (G), from the three regions of interest. The circle indicates the burned area.

#158016 - $15.00 USD Received 10 Nov 2011; revised 14 Jan 2012; accepted 16 Jan 2012; published 9 Feb 2012

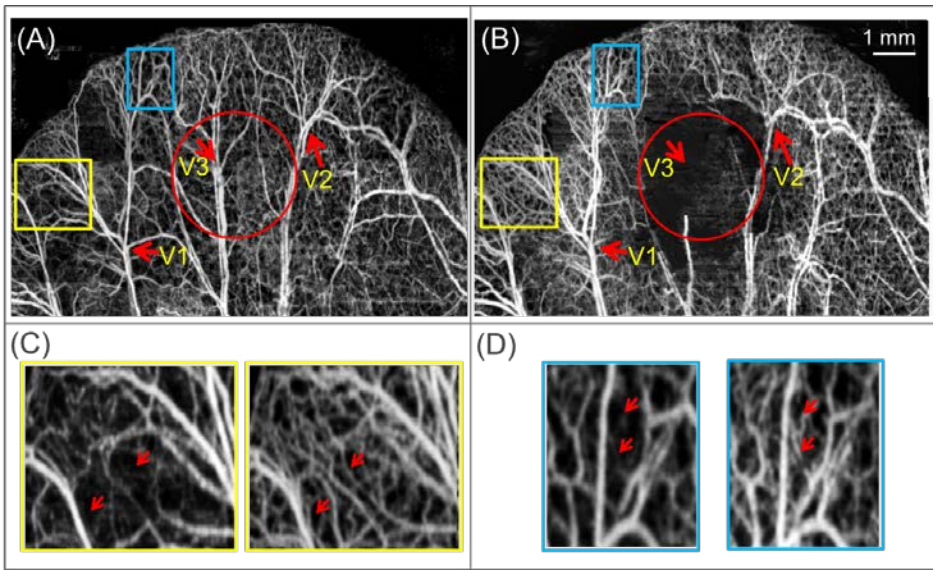

Fig. 4. Projection view image of the blood vessel network obtained by the OMAG method before (A) and after (B) the burn injury. The circle indicates the burned area and the arrows indicate the reference vessels from Fig. 2(B). Enlarged areas of the yellow (C) and blue (D) rectangles, where the left and right images belong to (A) and (B), respectively.

OMAG images; while in the LSI images they seem appear as single vessels due to its lower spatial resolution.

Figures 4(A) and 4(B) show the capillary vessels before and after the burn injury, respectively. Figure 4(B) contains an area in the middle where there are almost no visible vessels and capillaries (indicated by the red circle), where the injury occurred. Although the vessels may still be present, the flow has been stopped or significantly reduced. The smallest blood flow velocities that can be detected by OMAG are 4 μm/s [31]. Two regions (the yellow and blue rectangles) in the periphery of the burn area have been enlarged for direct comparison in Figs. 4(C) and 4(D). Qualitatively, it is noticed that there is an increase in capillary density after the injury (some representative capillaries have been marked with red arrows). Since the images were obtained within a few seconds of each other, we are certain that the appearance of new capillaries is not due to angiogenesis (new blood vessel formation). Instead, it is due to reserve capillaries that existed before the injury, but had no or minimum blood flow, and that has been recruited after the injury (known as capillary recruitment phenomena) [55,56].

Although the enlarged images (Figs. 4(C) and (D)) present a qualitative way for analyzing the images, we opted to use a quantitative method to evaluate the vessel density over a given area, i.e., vessel area density (VAD). VAD is a method that is developed to determine the ratio of the area that is occupied vessel and capillaries to a given region, thus it has a value between 0 and 1 [48]. To calculate the VAD, we first converted the OMAG images to black and white. This is accomplished by first applying a low pass filter that minimizes the image noise, followed by an adaptive threshold algorithm. On the black and white image we created a 64 × 64 pixels window (white solid box on the top left corner of Fig. 5(A)), and within that window we counted the number of white pixels, which was then divided by the total number of pixels in the window. The value was assigned to a middle pixel in the window. The window was moved across every pixel in the image to obtain the VAD image. For the pixels close to the borders of the images, a smaller window size was used to minimize artifacts.

Figures 5(A) and (B) show the VAD images multiplied by the black and white image, before and after the injury, respectively. These images enable the visualization of the regions of high and low vessel and capillary density. It is observed that the edges of the mouse pinna present a

#158016 - $15.00 USD Received 10 Nov 2011; revised 14 Jan 2012; accepted 16 Jan 2012; published 9 Feb 2012

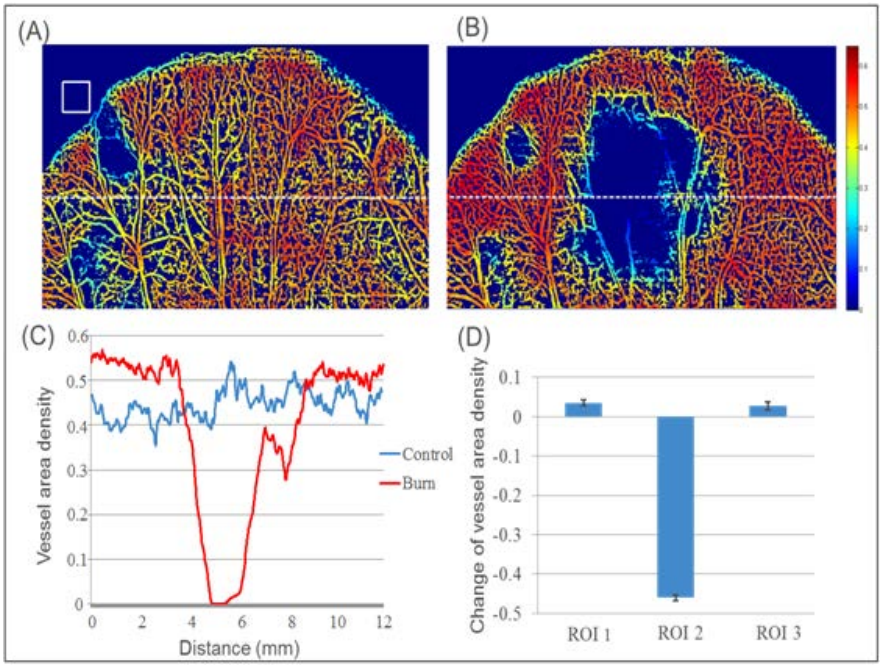

Fig. 5. Vessel area density map multiplied by the black and white projection view image of the blood vessel network obtained by the OMAG method before (A) and after (B) the burn injury. The white square in (A) is the window size used to calculate the VAD. (C) Vessel area density of the dashed line in (A) and (B). (D) Mean and standard deviation of the VAD for the three ROI's determined in Fig. 6.

slow decline in density due to the window covering regions both inside and outside of the mouse pinna. The VAD image after the injury shows a higher redness in the periphery of the burned area compared to the control image. We selected a region of interest indicated by a white dashed line. The VAD of the dashed line from the burn and control image is shown in Fig. 5(C). In the periphery of the injured area there is a higher VAD after the burn. However, within the injured site, there is a significant reduction of VAD. Although the injury was caused with a

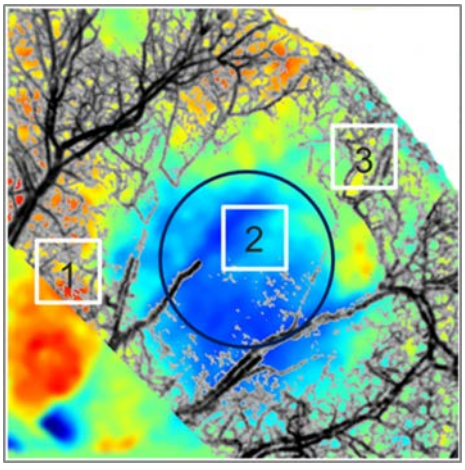

Fig. 6. Co-registered image of the change in blood flow image (Fig. 3A) with the projection view image of the blood vessel network obtained by the OMAG method after the injury (Fig. 4B). The color map is the same as in Fig. 3A. The grayscale of the OMAG image was inverted such that the blood vessels appear dark for better contrast.

#158016 - $15.00 USD Received 10 Nov 2011; revised 14 Jan 2012; accepted 16 Jan 2012; published 9 Feb 2012

2.5mm diameter bar, the reduction in VAD has a diameter greater than that value. Figure 5(D) presents the mean and standard deviation of the three regions of interest indicated in Fig. 3. These regions were easily identified by co-registering the LSI and OMAG images (Fig. 6), in which the gray color of the OMAG image was inverted such that the vessels appear black, to provide better contrast. From Fig. 5, it can be observed that there is an increase of VAD in the periphery regions, and a significant decrease of VAD within the injured region.

4. Conclusion

We have demonstrated that a multi-functional imaging system that combines 2-LSI with OMAG can be used to asses several important physiological parameters of the tissue blood perfusion status. The 2-LSI system revealed the relative change in blood flow, and the changes in the concentration of HbO, Hb and HbT. Concurrently, OMAG revealed high resolution images of small capillary networks, allowing for the quantification of the vessel area density and the observation of the capillary recruitment.

The results observed were presented with color coded maps, providing spatial information of the blood perfusion parameters. It has been determined that within a burn region, the flow rate, HbO and VAD decrease while the Hb and HbT slightly increase. On the other hand, the flow, Hb, HbT and VAD increases in certain regions of the periphery, while HbO decreases or has no change. These results are consistent with haemostasia occurring in the burn area and hyperaemia occurring in some of the surrounding regions. We also observe the phenomenon of capillary recruitment within a few minutes after the injury.

2-LSI has the advantages of imaging large areas, and its data acquisition time is fast. Currently, OMAG images have a small field of view and require several small images to be stitched together; however, it provides depth resolved high resolution images. In general, the combination of both techniques delivers a valuable platform for better understanding the functional hemodynamic and morphology changes of the vasculatures, which will provide useful information that may benefit the diagnosis and treatment of diseases that have vascular involvement.

Acknowledgments

This work was supported in part by research grants from the National Institutes of Health (HL093140, HL093140S, EB009682, and DC010201) and the American Heart Association (0855733G). The content is solely the responsibility of the authors and does not necessarily represent the official views of grant giving bodies.

#158016 - $15.00 USD Received 10 Nov 2011; revised 14 Jan 2012; accepted 16 Jan 2012; published 9 Feb 2012